High-Time-Resolution Microspectrometer Based on Phase-Change Materials

Xiong Deng,[1,2] Ximin Tian,[3] Lirong Ren,[2] Jiangtao Liu,[1,2,*] and Zhi-Yuan Li[1,4,†]

[1] *School of Physics and Optoelectronics, South China University of Technology, Guangzhou 510640, China*
[2] *College of Mechanical and Electrical Engineering, Guizhou Minzu University, Guiyang 550025, China*
[3] *School of Materials Science and Engineering, Zhengzhou University of Aeronautics, Zhengzhou 450046, China*
[4] *State Key Laboratory of Luminescent Materials and Devices, South China University of Technology, Guangzhou 510640, China*

(Received 29 July 2022; revised 12 October 2022; accepted 16 November 2022; published 12 December 2022)

The application of graphene–photonic crystal microcavity structures with phase-change-material layers in spectral analysis is studied. It is found that selective absorption of different wavelengths of light can be realized by changing the crystallinity of the phase-change material, so that different wavelengths of light can be separated and measured in the time domain to perform spectral analysis. Since the phase-transition time of phase-change materials is very fast, this spectral analysis can be done with submicrosecond time resolution. This kind of spectral-analysis device has a simple structure and can be integrated with a chip. It has important prospects for application in the fields of biological molecular recognition, biological sensing, and chemical analysis.

DOI: 10.1103/PhysRevApplied.18.064032

I. INTRODUCTION

Spectrometers, which can characterize the characteristic spectra of substances and analyze their composition and structure, are among the most widely used analytical tools in scientific research and in industry. However, traditional spectrometers perform spectral analysis mainly with prisms [1], gratings [2,3], or structures similar to the Michelson interferometer [4]. Spectrometers can provide ultrahigh resolution and a wide spectral-measurement range. However, traditional spectrometers have a complex structure, large volume, and poor portability [5,6]. With progress in emerging technologies such as biotechnology and trace analysis, rapid analysis of microsamples is becoming more and more important. Thus, miniaturization of analytical instruments and integration with chips has become a development trend [7–10].

In order to reduce the size of the spectrometer and integrate it with a chip, a variety of spectral-analysis techniques based on different principles have been proposed, including an on-chip Fourier transform spectrometer [11,12], an integrated filter array [13–15], a wedge microcavity [16,17], the use of on-chip disordered structural light scattering [18,19], a two-dimensional absorption filter array composed of continuously tunable colloidal quantum dots [20,21], a nanowire detector array with a gradually changing band gap [22–24], an ultracompact photonic crystal nanobeam cavity array [25,26], photonic crystal slabs [27,28], and metasurfaces [29,30].

However, traditional microspectrometers separate and detect light in space mainly by use of a strong dispersion medium or a detection array. Because of the limitation on dispersive power, it is difficult to further reduce the size of a traditional spectrometer. In this paper, a one-dimensional photonic crystal optical microcavity containing a phase-change material and graphene is studied and used for spectral analysis. The resonant frequency of the microcavity is rapidly regulated by a rapid change of the dielectric constant of the phase-change material during the phase-change process [31–37]. This fast regulation can separate and selectively detect different wavelengths of light on a submicrosecond time scale [38–40], thus achieving high-time-resolution spectroscopy. Separating and measuring light of different wavelengths in the time domain rather than the spatial domain requires a smaller spatial size, which is beneficial for the miniaturization of the spectrometer. This kind of spectrometer has a simple structure, and the fabrication process can be integrated with that of a chip.

II. STRUCTURE AND METHOD

The structure of the graphene–photonic crystal microcavity composite with phase-change-material layers studied in this paper, shown in Fig. 1(a), is $(AB)^M AC_1C_2\mathrm{G}C_2C_1(AB)^N$. A and B are periodically arranged Si and SiO_2, which are alternately placed to form two distributed Bragg reflectors. C_1 is a Sb_2S_3 phase-change-material layer, C_2 is a SiO_2 insulating isolation layer, G is single-layer

*jtliu@semi.ac.cn
†phzyli@scut.edu.cn

graphene, and M and N are the periods. The thicknesses of the SiO_2 layer and Si layer in the distributed Bragg reflector are $d_A = \lambda_C/4n_A$ and $d_B = \lambda_C/4n_B$, respectively. The central wavelength is $\lambda_C = 1.310$ μm, the refractive index of the Si is 3.50, and the refractive index of the SiO_2 is 1.47 [41]. The phase-change-material layer is Sb_2S_3, which is a low-loss phase-change material and has a very low loss at 1550 nm in the communication band. The imaginary part of the refractive index κ is less than 10^{-5}, and the real part of the refractive-index change Δn is 0.6 during the amorphous-to-crystalline phase transition [42]. The phase-change material Sb_2S_3 has little light absorption at this wavelength, and so the influence of the phase change on the resistance will be much larger than that of light on the resistance. Therefore, adding an additional photoelectric conversion layer can improve the detection accuracy. Here, the middle photoelectric conversion layer is single-layer graphene. The photoelectric conversion efficiency of single-layer or multilayer graphene in the infrared light band changes little with wavelength [43–46]. Graphene requires no lattice matching and is easy to integrate. However, the photoelectric conversion efficiency of graphene is lower than that of some traditional semiconductor materials, e.g., InP/(In, Ga)As/InP quantum wells [47]. If a highly sensitive spectrometer is required, an InP/(In, Ga)As/InP quantum well can be used instead of graphene. The thickness of the graphene layer d_g is 0.335 nm [48]. In the visible and near-infrared bands, the complex refractive index of monolayer graphene n_g is $3.0 + \zeta_g\,(\lambda/3)\,i$, where $\zeta_g = 5.446$ μm^{-1}, and λ is the wavelength of the incident light [49]. Both sides of the graphene are separated from the surrounding phase-change material by a SiO_2 insulation layer with a thickness d_{C_2} to reduce the influence of the photocurrent and of deformation of the phase-change layer, taking $d_{C_2} = 10$ nm in the calculation. The microspectrometer is a layered stacked structure with a thickness of 2.905 μm, which is compatible with mature semiconductor device manufacturing processes and convenient for integrating with a chip.

The light absorption of graphene is calculated using the transfer-matrix method [50–52]. Compared with the finite-difference time-domain method, the transfer-matrix method has the advantage of fast computational speed, high accuracy, and low error. The electric field in layer l is

$$E_l(z) = A_l e^{-\omega n_{lr}\Delta z_l/c} e^{i\omega n_{li}\Delta z_l/c} + B_l e^{\omega n_{lr}\Delta z_l/c} e^{-i\omega n_{li}\Delta z_l/c}, \tag{1}$$

and the magnetic field is

$$H_l(z) = \gamma_l\left(A_l e^{-\omega n_{lr}\Delta z_l/c} e^{i\omega n_{li}\Delta z_l/c} - B_l e^{\omega n_{lr}\Delta z_l/c} e^{-i\omega n_{li}\Delta z_l/c}\right), \tag{2}$$

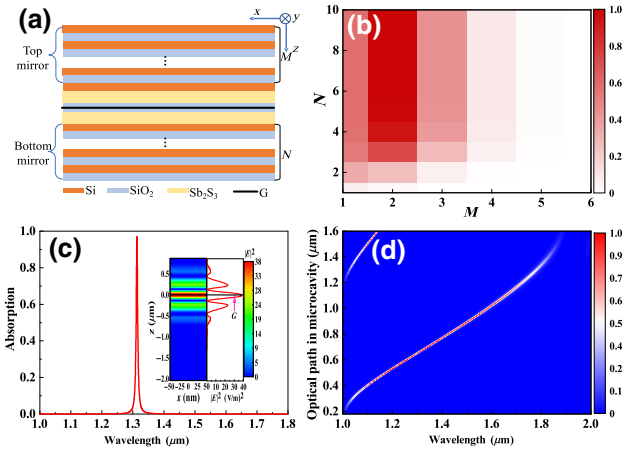

FIG. 1. (a) Schematic diagram of graphene–photonic crystal microcavity structure with phase-change-material layers. (b) Contour map of absorption rate of graphene as a function of the number of periods in the distributed-Bragg-reflector mirrors on both sides of the microcavity. (c) Absorption rate of graphene as a function of wavelength. The inset shows a distribution map of the electric field in the microcavity at the resonance wavelength; the black solid line is the position of the graphene. (d) Contour map of absorption rate of graphene as a function of wavelength and microcavity optical path.

where $\Delta z_l = z - z_l$, z_l is the location of the interface between layer $(l-1)$ and layer l, A_l and B_l are the electric field amplitudes of the light waves propagating along the positive and negative directions, respectively, at z_l, ω is the circular frequency, c is the light velocity, n_{lr} and n_{li} are the real and imaginary parts, respectively, of the refractive index of the medium in layer l, $\gamma_l = \sqrt{\varepsilon_l/\mu_l}$, and ε_l and μ_l are the dielectric constant and permeability, respectively, of the medium in the layer l. From the boundary conditions, the relationship between the two positive and negative electric field amplitudes in layer l of the photonic crystal and the first layer irradiated by the incident light wave is as follows:

$$\begin{pmatrix} A_l \\ B_l \end{pmatrix} = T_{l-1} \times \cdots \times T_1 \begin{pmatrix} A_0 \\ B_0 \end{pmatrix} = \begin{pmatrix} T_{11} & T_{12} \\ T_{21} & T_{22} \end{pmatrix} \times \begin{pmatrix} A_0 \\ B_0 \end{pmatrix}. \tag{3}$$

The absorption rate of the medium in layer l can be calculated from the Poynting vector [53,54]:

$$\varphi_l = \left(S_{(l-1)i} - S_{(l+1)i} - S_{(l-1)o} + S_{(l+1)o}\right)/S_{0i}, \tag{4}$$

where $S_{(l-1)i}$ and $S_{(l-1)o}$ denote the Poynting vectors of the incident and outgoing light waves in layer $(l-1)$, $S_{(l+1)i}$ and $S_{(l+1)o}$ denote the Poynting vectors of the incident and outgoing light waves in layer $(l+1)$, and S_{0i} denotes the Poynting vector of the incident light. In

addition, $S_{(l-1)i} = \beta_{l-1}A_{l-1}^2$, $S_{(l-1)o} = \beta_{l-1}B_{l-1}^2$, $S_{(l+1)i} = \beta_{l+1}A_{l+1}^2$, and $S_{(l+1)o} = \beta_{l+1}B_{l+1}^2$ for the TE mode, and $\beta_{l-1} = \sqrt{\varepsilon_{l-1}/\mu_0}$ and $\beta_{l+1} = \sqrt{\varepsilon_{l+1}/\mu_0}$, where ε_{l-1} and ε_{l+1} are the dielectric constants of layer $(l-1)$ and layer $(l+1)$, and μ_0 is the vacuum permeability.

III. NUMERICAL RESULTS

Early studies have shown that an asymmetric photonic crystal microcavity, that is, one in which M is not equal to N, is more conducive to enhancing the optical absorption of graphene [55–58], which is well proved by our calculation results [Fig. 1(b)]. When $M = 2$ and $N = 6$, the light absorption rate is high. In the following calculations, $M = 2$ and $N = 6$ are used.

The change of the graphene absorption rate with wavelength is shown in Fig. 1(c). The peak value of the absorption peak is 0.982, and the full width at half maximum (FWHM) of the absorption peak is 5.20 nm. The ratio of the square of the modulus of the graphene electric field intensity to the square of the modulus of the incident electric field intensity $\left(|E_g|^2 / |E_i|^2\right)$ equals 37.8, which greatly enhances the optical absorption of the graphene. Similarly to other interference structures, the resonant wavelength of the absorption peak can be controlled by changing the optical path of the microcavity defect layer, which means that the central wavelength of the absorption peak increases with an increase in the optical path of the microcavity, as shown in Fig. 1(d). Except at the edge of the photonic band gap, the attenuation of the absorption peak is not obvious.

In particular, a phase transition between the amorphous (a-Sb_2S_3) and crystalline (c-Sb_2S_3) states in Sb_2S_3 thin films in a microcavity can be induced by pulsed current heating or laser irradiation. Moreover, Sb_2S_3 has intermediate states with different crystallinities between the amorphous (a-Sb_2S_3) and crystalline (c-Sb_2S_3) states [59,60], so different-power excitation sources such as laser pulses can be used to control the crystallinity of Sb_2S_3. The effective dielectric constant of Sb_2S_3 in the intermediate state can be obtained from the Lorenz relationship and the Brookmann mixing rule [61,62]:

$$\frac{\varepsilon_{\text{eff}}(\lambda) - 1}{\varepsilon_{\text{eff}}(\lambda) + 2} = \eta \frac{\varepsilon_c(\lambda) - 1}{\varepsilon_c(\lambda) + 2} + (1 - \eta) \frac{\varepsilon_a(\lambda) - 1}{\varepsilon_a(\lambda) + 2}, \quad (5)$$

where $\varepsilon_c(\lambda)$ and $\varepsilon_a(\lambda)$ are the wavelength-dependent dielectric constants of Sb_2S_3 in the crystalline and amorphous states, respectively, and η is the crystallinity of crystalline Sb_2S_3. The energy density required for the conversion of the phase-change material from the amorphous state to the crystalline state is 0.029 fJ/nm^3 [63], which is far less than the maximum light intensity that graphene can withstand and will not affect the performance of the graphene.

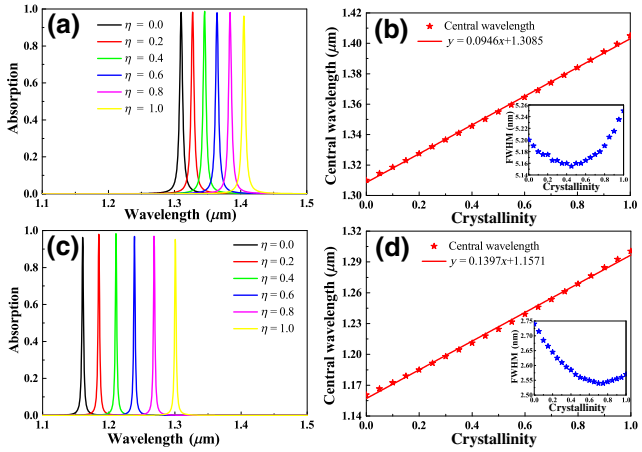

FIG. 2. Light absorption rate of graphene as a function of wavelength for different crystallinities when the optical path in the defect layer is (a) $\lambda_c/2$ and (c) $5\lambda_c/4$. Change of central wavelength of absorption peak with crystallinity of phase-change material when the optical path in the defect layer is (b) $\lambda_c/2$ and (d) $5\lambda_c/4$. The illustration shows the relationship between the FWHM of the absorption peak and the crystallinity.

The absorption rate of graphene for different crystallinities is shown in Fig. 2(a). When the crystallinity of the phase-change material increases, its refractive index increases. The resonant condition of the microcavity can be described by $2n_pLk = 2m_p\pi$, where n_p is the refractive index of the medium, m_p is an integer, L is the thickness of the microcavity, and k is the wave vector of the light, and a resonant wavelength $\lambda \propto n_p$ in the microcavity is obtained. The increase in the refractive index increases the optical path in the defect layer in the microcavity and the resonant wavelength of the microcavity. So, the absorption peak of the graphene in the microcavity is redshifted and selective absorption of light at different wavelengths is realized. But the peak value of the absorption peak changes little, remaining close to the maximum absorption rate (0.988).

When the crystallinity changes from 0 to 100% , the central wavelength of the absorption peak changes from 1.31 to 1.41 μm, and the wavelength range is 0.1 μm [Fig. 2(b)]. The central wavelength of the absorption peak is linearly related to the crystallinity of the phase-change material, and the correlation coefficient is as high as 0.999. In this way, the crystallinity and the absorption wavelength can be put into one-to-one correspondence to facilitate the design of a spectrometer. The relative variation of the FWHM of the absorption peak with crystallinity is not obvious, as shown in the illustration in Fig. 2(b). The minimum FWHM is 5.16 nm, and the maximum FWHM is 5.25 nm, which has a high wavelength resolution and good consistency. An appropriate increase in the thickness of the microcavity can further improve the influence of crystallinity on the position of the absorption peak. When

the thickness of the microcavity increases, the same crystallinity changes lead to higher optical-path changes, so that the absorption peak moves more, as shown in Fig. 2(c). During the phase transition, the central wavelength of the absorption peak changes from 1.16 to 1.30 μm, and the wavelength-adjustment range becomes 0.14 μm, with an increase of 40% [Fig. 2(d)]. In a spectrometer, the tuning range is important. If the tuning range is too small, the device cannot be used as a spectrometer. At the same time, a longer cavity can improve the Q value, so that the FWHM of the absorption peak becomes smaller; the minimum FWHM is 2.54 nm, which can improve the resolution of the spectrometer. In addition, when multiple photonic crystal microcavity arrays with different initial optical paths are integrated into the device, combined with a band-pass filter, the spectral measurement range can be extended to the full band of near-infrared spectroscopy.

In addition to using different-power excitation sources to control the crystallinity of the Sb_2S_3 in the stable state, the crystallinity of the phase-change material during the crystallization process can also be changed continuously by a rapid pump, and the change rate is very fast. By fitting the experimental results, the change of the crystallinity of the phase-change material Sb_2S_3 with time is obtained, and the phase-change time is about 100 ns [inset of Fig. 3(a)] [63]. The rapid change of the crystallinity of the phase-change material with time makes its refractive index and the optical path of the microcavity vary rapidly with time, which leads to a change of the central wavelength of the absorption peak with time, as shown in Fig. 3(a). In this way, different wavelengths of light can be separated in time, so as to realize high-time-resolution measurement of the spectrum. The resistance of the phase-change-material layer can be measured in real time to monitor the crystallinity of the layer.

The proposed structure is used to simulate a time-resolved fluorescence spectrometric measurement commonly used in biochemical analysis to better reflect the application of phase-change materials in time-resolved spectrometric measurements [64–66]. The fluorescence spectra emitted by substances usually have a Lorentzian line shape and decay exponentially with time. So, at a time $t = t_{pl}$, the luminescence intensity of the spectrum can be written as [67]

$$P_e\left(\lambda, t_{pl}\right) = \frac{1}{\pi}\left(\frac{\alpha_L}{\left(\lambda-\lambda_0\right)^2-\alpha_L^2}\right) e^{-t_{pl}/\tau}, \qquad (6)$$

where the spectral center wavelength is $\lambda_0 = 1.230$ μm, half of the FWHM is $\alpha_L = 7.5$ nm, and the attenuation coefficient is $\tau = 1$ ms. The spectral curves of the fluorescence at different times t_{pl} are shown in Fig. 3(b). After the fluorescence material has been pumped by the pump light and after different time delays Δt_{pump}, the phase change of the phase-change material is driven by a fast excitation

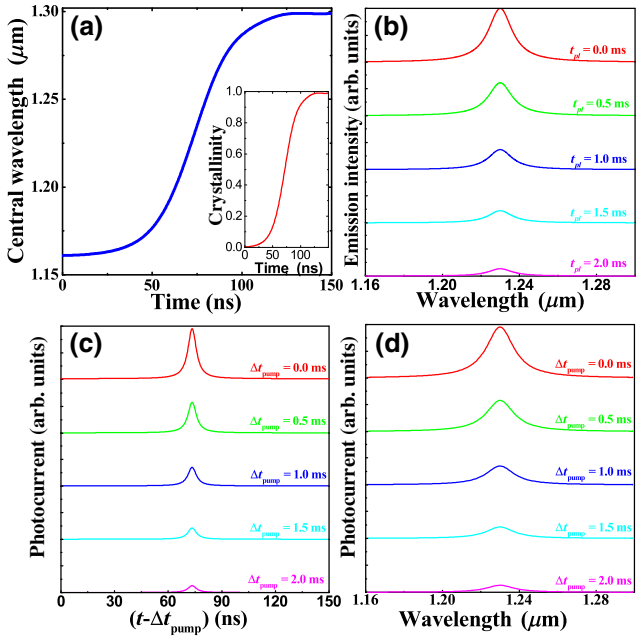

FIG. 3. (a) Central wavelength of graphene absorption peak as a function of time. The inset shows the relationship between the crystallinity of Sb_2S_3 and time. (b) Lorentzian-line-shape fluorescence spectral curve with exponential decay over time. (c) Variation curve of photocurrent of graphene with time for different pump delays. (d) Reconstructed spectral curves for different pump delays.

source. During the phase change, the graphene selectively absorbs incident light of different wavelengths over the following period of time, and its light-absorption rate can be expressed as $\varphi\left(\lambda, t-\Delta t_{\text{pump}}\right)$. Experimental results show that the photocurrent in graphene is linearly related to the absorption rate of the graphene [48], and that the light absorbed by the graphene can be effectively converted into a photocurrent. Assuming κ_g is the photoelectric conversion efficiency of the graphene, the variation with time of the measured photocurrent in the photoelectric conversion layer is given by

$$I\left(\Delta t_{\text{pump}}, t\right) = \kappa_g \int P_e\left(\lambda, t\right) \varphi\left(\lambda, t-\Delta t_{\text{pump}}\right) d\lambda. \qquad (7)$$

The photocurrent-versus-time curves of the graphene for different pump delays are calculated, as shown in Fig. 3(c). Time-resolved spectra can be reconstructed by use of the time-wavelength correspondence transformation. The reconstruction of the spectrum can be done by a method of computational reconstruction with high accuracy [23,25,26]; however, since the absorption spectrum has a unimodal structure and the FWHM is very small, we use a coordinate-transformation method to reconstruct the spectral curve. Using the correspondence between the phase-change time and the absorption peak wavelength, the curve of the photocurrent versus phase-change time is

converted into a curve of the photocurrent versus wavelength, that is, a spectral curve, as shown in Fig. 3(d). Comparing Figs. 3(b) and 3(d), it is found that the spectral curves are similar, which verifies that the method can achieve spectral analysis. The time resolution is equivalent to the crystallization rate of the phase-change material. For Sb_2S_3, the time-response speed of the spectral analysis is in the order of 100 ns, and the time resolution of the spectrometer can reach the submicrosecond level.

The optical absorption of the phase-change-material layer (Sb_2S_3) is very small in the band range we study. But, if the spectral detection needs to be extended to different wavelength ranges, different phase-change materials are needed. In such wavelength ranges, some phase-change materials have small absorption. So, we study the influence of the absorption of the phase-change material on spectral analysis. When the light absorption of the phase-change material increases, the light absorption of the graphene decreases. At the same time, the increase in absorption reduces the Q value of the microcavity and increases the FWHM. When the imaginary part of the refractive index n_{li} increases from 0 to 0.05, the peak value of the absorption peak decreases significantly, from 0.982 to 0.0482. The FWHM of the absorption peak increases from 5.20 to 23.50 nm, as shown in Fig. 4(a). Thus, the optical absorption of the phase-change material greatly reduces the performance of the spectrometer.

The influence of the phase-change material can be reduced by adding a silicon layer between the insulating isolation layer and the phase-change-material layer. This is because the light absorption occurs mainly at places with a strong field strength, where the introduction of a silicon layer with small absorption can weaken the absorption of the phase-change material and increase the Q value of the microcavity. In order to ensure that the position of the absorption peak is unchanged, the thickness of the phase-change-material layer needs to be reduced after adding the silicon layer. When $n_{li} = 0.03$, the peak value of the absorption peak increases with an increase in the thickness of the silicon layer. When the thickness of the silicon layer is 10 nm, the peak value of the absorption peak is 0.152, and the FWHM is 13.3 nm. When the thickness of the silicon layer is 50 nm, the peak value of the absorption peak is 0.674 and the FWHM is 5.85 nm, as shown in Fig. 4(b). The peak value of the absorption peak increases by 3.45 times and the FWHM decreases by 55.9%. After the addition of silicon layers with different thicknesses, the changes in the peak value and FWHM of the absorption peak with the crystallinity of the phase-change material are shown in Figs. 4(c) and 4(d). For different crystallinities, the peak value of the graphene absorption peak increases with an increase in the thickness of the silicon layer, and the FWHM decreases with an increase in the thickness of the silicon layer, which indicates that the spectral resolution is greatly improved after addition of the silicon layer. In addition, the peak value and the FWHM of the absorption peak are almost unaffected by the change of crystallinity, and the time resolution of the spectrometer is maintained.

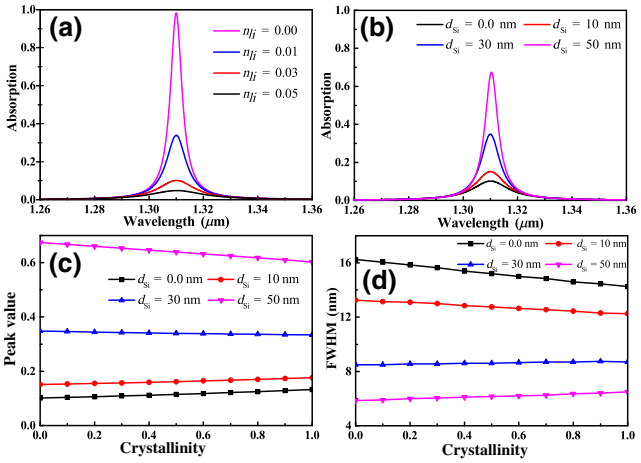

FIG. 4. (a) Variation of absorption rate of graphene with wavelength for different values of the imaginary part of the refractive index of the phase-change material. (b) Variation of absorption rate of graphene with wavelength for different silicon layer thicknesses d_{Si} when the imaginary part of the refractive index of the phase-change material $n_{li} = 0.03$. Variation of peak value (c) and FWHM (d) of absorption peak with the crystallinity of the phase-change material for different silicon layer thicknesses d_{Si}.

IV. CONCLUSIONS

In this paper, the application of graphene–photonic crystal microcavity structures with phase-change-material layers in spectral analysis is studied. The results show that the change of crystallinity of phase-change materials can be used to realize the separation and measurement of different wavelengths of light in the time domain rather than the spatial domain. The wavelength-adjustment range is 0.14 μm, and the minimum FWHM is 2.54 nm. Because the phase-transition time of the phase-change material is in the order of 100 ns, submicrosecond time resolution can be achieved with high spectral resolution. In addition, adding a silicon layer between the insulating isolation layer and the phase-change-material layer can reduce the detrimental effect of the absorption of the phase-change material. When the thickness of the silicon layer is increased to 50 nm, the peak value of the absorption peak increases by 3.45 times and the FWHM decreases by 55.9%. The spectrometer has a simple structure, and the material is compatible with the production processes of mature semiconductor devices and convenient for chip integration. This integratable and high-time-resolution microspectrometer has important prospects for application in biomolecular recognition, biosensing, and chemical analysis.

ACKNOWLEDGMENTS

The authors are grateful for financial support from the National Natural Science Foundation of China (Grants No. 11974119, No. 12004347, and No. 62174040), the Science and Technology Project of Guangdong (Grant No. 2020B010190001), the Guangdong Innovative and Entrepreneurial Research Team Program (Grant No. 2016ZT06C594), the National Key R&D Program of China (Grant No. 2018YFA 0306200), the Scientific and Technological Project in Henan Province (Grants No. 212102310255, No. 202102310535, and No. 222102210063), the Aeronautical Science Foundation of China (Grants No. 2020Z073055002 and No. 2019ZF055002), the Innovative Research Team (in Science and Technology) in the University of Henan Province (Grant No. 22IRTSTHN004), and the 13th batch of the Outstanding Young Scientific and Technological Talents Project in Guizhou Province (Grant No. [2021]5618).

[1] C. Yang, K. Shi, P. Edwards, and Z. Liu, Demonstration of a PDMS based hybrid grating and Fresnel lens (G-Fresnel) device, Opt. Express **18**, 23529 (2010).

[2] R. Cheng, C.-L. Zou, X. Guo, S. Wang, X. Han, and H. X. Tang, Broadband on-chip single-photon spectrometer, Nat. Commun. **10**, 1 (2019).

[3] X. Ma, M. Li, and J.-J. He, CMOS-compatible integrated spectrometer based on echelle diffraction grating and MSM photodetector array, IEEE Photonics J. **5**, 6600807 (2013).

[4] A. Fathy, Y. M. Sabry, S. Nazeer, T. Bourouina, and D. A. Khalil, On-chip parallel Fourier transform spectrometer for broadband selective infrared spectral sensing, Microsyst. Nanoeng. **6**, 1 (2020).

[5] Z. Yang, T. Albrow-Owen, W. Cai, and T. Hasan, Miniaturization of optical spectrometers, Science **371**, eabe0722 (2021).

[6] A. Z. Subramanian, E. Ryckeboer, A. Dhakal, F. Peyskens, A. Malik, B. Kuyken, H. Zhao, S. Pathak, A. Ruocco, and A. De Groote, *et al.*, Silicon and silicon nitride photonic circuits for spectroscopic sensing on-a-chip, Photon. Res. **3**, B47 (2015).

[7] C. P. Bacon, Y. Mattley, and R. DeFrece, Miniature spectroscopic instrumentation: Applications to biology and chemistry, Rev. Sci. Instrum. **75**, 1 (2004).

[8] D. Rodrigo, O. Limaj, D. Janner, D. Etezadi, F. J. G. de Abajo, V. Pruneri, and H. Altug, Mid-infrared plasmonic biosensing with graphene, Science **349**, 165 (2015).

[9] D. M. Kita, B. Miranda, D. Favela, D. Bono, J. Michon, H. Lin, T. Gu, and J. Hu, High-performance and scalable on-chip digital Fourier transform spectroscopy, Nat. Commun. **9**, 1 (2018).

[10] S. Babin, A. Bugrov, S. Cabrini, S. Dhuey, A. Goltsov, I. Ivonin, E.-B. Kley, C. Peroz, H. Schmidt, and V. Yankov, Digital optical spectrometer-on-chip, Appl. Phys. Lett. **95**, 041105 (2009).

[11] M. C. M. M. Souza, A. Grieco, N. C. Frateschi, and Y. Fainman, Fourier transform spectrometer on silicon with thermo-optic non-linearity and dispersion correction, Nat. Commun. **9**, 665 (2018).

[12] L. Zhang, J. Chen, C. Ma, W. Li, Z. Qi, and N. Xue, Research progress on on-chip Fourier transform spectrometer, Laser Photon. Rev. **15**, 2100016 (2021).

[13] S.-W. Wang, C. Xia, X. Chen, W. Lu, H. Wang, W. Zheng, and T. Zhang, Concept of a high-resolution miniature spectrometer using an integrated filter array, Opt. Lett. **32**, 632 (2007).

[14] Y. Horie, A. Arbabi, E. Arbabi, S. M. Kamali, and A. Faraon, Wide bandwidth and high resolution planar filter array based on DBR-metasurface-DBR structures, Opt. Express **24**, 11677 (2016).

[15] E. Huang, Q. Ma, and Z. Liu, Etalon array reconstructive spectrometry, Sci. Rep. **7**, 1 (2017).

[16] T. Jeon, A. Nateghi, W. M. Jones, C. Choi, J. P. Cardenas, C. Ross, and A. Scherer, Development of a compact and robust mid-infrared spectrometer by using a silicon/air hyperspectral filter, ACS Photonics **9**, 68 (2022).

[17] M. W. Pruessner, T. H. Stievater, and W. S. Rabinovich, Integrated waveguide Fabry-Perot microcavities with silicon/air Bragg mirrors, Opt. Lett. **32**, 533 (2007).

[18] B. Redding, S. F. Liew, R. Sarma, and H. Cao, Compact spectrometer based on a disordered photonic chip, Nat. Photonics **7**, 746 (2013).

[19] W. Hartmann, P. Varytis, H. Gehring, N. Walter, F. Beutel, K. Busch, and W. Pernice, Waveguide-integrated broadband spectrometer based on tailored disorder, Adv. Opt. Mater. **8**, 1901602 (2020).

[20] J. Bao and M. G. Bawendi, A colloidal quantum dot spectrometer, Nature **523**, 67 (2015).

[21] X. Zhu, L. Bian, H. Fu, L. Wang, B. Zou, Q. Dai, J. Zhang, and H. Zhong, Broadband perovskite quantum dot spectrometer beyond human visual resolution, Light: Sci. Appl. **9**, 1 (2020).

[22] Z. Yang, T. Albrow-Owen, H. Cui, J. Alexander-Webber, F. Gu, X. Wang, T.-C. Wu, M. Zhuge, C. Williams, and P. Wang, *et al.*, Single-nanowire spectrometers, Science **365**, 1017 (2019).

[23] J. Meng, J. J. Cadusch, and K. B. Crozier, Detector-only spectrometer based on structurally colored silicon nanowires and a reconstruction algorithm, Nano Lett. **20**, 320 (2019).

[24] L. Kong, Q. Zhao, H. Wang, J. Guo, H. Lu, H. Hao, S. Guo, X. Tu, L. Zhang, and X. Jia, *et al.*, Single-detector spectrometer using a superconducting nanowire, Nano Lett. **21**, 9625 (2021).

[25] Z. Cheng, Y. Zhao, J. Zhang, H. Zhou, D. Gao, J. Dong, and X. Zhang, Generalized modular spectrometers combining a compact nanobeam microcavity and computational reconstruction, ACS Photonics **9**, 74 (2021).

[26] J. Zhang, Z. Cheng, J. Dong, and X. Zhang, Cascaded nanobeam spectrometer with high resolution and scalability, Optica **9**, 517 (2022).

[27] Z. Wang, S. Yi, A. Chen, M. Zhou, T. S. Luk, A. James, J. Nogan, W. Ross, G. Joe, and A. Shahsafi, *et al.*, Single-shot on-chip spectral sensors based on photonic crystal slabs, Nat. Commun. **10**, 1 (2019).

[28] T. Yang, C. Xu, H.-p. Ho, Y.-y. Zhu, X.-h. Hong, Q.-j. Wang, Y.-c. Chen, X.-a. Li, X.-h. Zhou, and M.-d. Yi, *et al.*,

Miniature spectrometer based on diffraction in a dispersive hole array, Opt. Lett. **40**, 3217 (2015).
[29] B. Craig, V. R. Shrestha, J. Meng, J. J. Cadusch, and K. B. Crozier, Experimental demonstration of infrared spectral reconstruction using plasmonic metasurfaces, Opt. Lett. **43**, 4481 (2018).
[30] M. Faraji-Dana, E. Arbabi, A. Arbabi, S. M. Kamali, H. Kwon, and A. Faraon, Compact folded metasurface spectrometer, Nat. Commun. **9**, 1 (2018).
[31] M. Wuttig, H. Bhaskaran, and T. Taubner, Phase-change materials for non-volatile photonic applications, Nat. Photonics **11**, 465 (2017).
[32] M. Rudé, V. Mkhitaryan, A. E. Cetin, T. A. Miller, A. Carrilero, S. Wall, F. J. G. de Abajo, H. Altug, and V. Pruneri, Ultrafast and broadband tuning of resonant optical nanostructures using phase-change materials, Adv. Opt. Mater. **4**, 1060 (2016).
[33] X. Tian, J. Xu, K. Xu, Y. Qian, X. Ma, P. Yang, X. Duan, P. Ding, and Z.-Y. Li, Phase-change reconfigurable metasurface for broadband, wide-angle, continuously tunable and switchable cloaking, Opt. Express **29**, 5959 (2021).
[34] H. Hillmer, C. Woidt, A. Istock, A. Kobylinskiy, D. T. Nguyen, N. Ahmed, R. Brunner, and T. Kusserow, Role of nanoimprint lithography for strongly miniaturized optical spectrometers, Nanomaterials **11**, 164 (2021).
[35] C. Williams, N. Hong, M. Julian, S. Borg, and H. J. Kim, Tunable mid-wave infrared Fabry-Perot bandpass filters using phase-change GeSbTe, Opt. Express **28**, 10583 (2020).
[36] J. Xu, X. Tian, P. Ding, K. Xu, and Z.-Y. Li, $Ge_2Sb_2Se_4Te_1$-based multifunctional metalenses for polarization-independent, switchable and dual-mode focusing in the mid-infrared region, Opt. Express **29**, 44227 (2021).
[37] X. Shi, C. Chen, S. Liu, and G. Li, Nonvolatile, reconfigurable and narrowband mid-infrared filter based on surface lattice resonance in phase-change $Ge_2Sb_2Te_5$, Nanomaterials **10**, 2530 (2020).
[38] T. Cao and M. Cen, Fundamentals and applications of chalcogenide phase-change material photonics, Adv. Theory Simul. **2**, 1900094 (2019).
[39] C. Ríos, P. Hosseini, R. A. Taylor, and H. Bhaskaran, Color depth modulation and resolution in phase-change material nanodisplays, Adv. Mater. **28**, 4720 (2016).
[40] Y. Zhang, J. B. Chou, J. Li, H. Li, Q. Du, A. Yadav, S. Zhou, M. Y. Shalaginov, Z. Fang, and H. Zhong, *et al.*, Broadband transparent optical phase change materials for high-performance nonvolatile photonics, Nat. Commun. **10**, 1 (2019).
[41] *Handbook of Optical Constants of Solids*, edited by E. D. Palik (Academic Press, New York, 1991), Vol. 2, p. 555.
[42] M. Delaney, I. Zeimpekis, D. Lawson, D. W. Hewak, and O. L. Muskens, A new family of ultralow loss reversible phase-change materials for photonic integrated circuits: Sb_2S_3 and Sb_2Se_3, Adv. Funct. Mater. **30**, 2002447 (2020).
[43] F. Wang, Y. Zhang, C. Tian, C. Girit, A. Zettl, M. Crommie, and Y. R. Shen, Gate-variable optical transitions in graphene, Science **320**, 206 (2008).
[44] Z. Z. Zhang, K. Chang, and F. M. Peeters, Tuning of energy levels and optical properties of graphene quantum dots, Phys. Rev. B **77**, 235411 (2008).
[45] D. Zhang, D.-B. Zhang, F. Yang, H.-Q. Lin, H. Xu, and K. Chang, Interface engineering of electronic properties of graphene/boron nitride lateral heterostructures, 2D Mater. **2**, 041001 (2015).
[46] M. Zhou, C. Zhou, K. Luo, W. Li, J. Liu, Z. Liu, and Z. Wu, Ultrawide bandwidth and sensitive electro-optic modulator based on a graphene nanoelectromechanical system with superlubricity, Carbon **176**, 228 (2021).
[47] Y.-Q. Fang, W. Chen, T.-H. Ao, C. Liu, L. Wang, X.-J. Gao, J. Zhang, and J.-W. Pan, InGaAs/PnP single-photon detectors with 60% detection efficiency at 1550 nm, Rev. Sci. Instrum. **91**, 083102 (2020).
[48] M. Furchi, A. Urich, A. Pospischil, G. Lilley, K. Unterrainer, H. Detz, P. Klang, A. M. Andrews, W. Schrenk, and G. Strasser, *et al.*, Microcavity-integrated graphene photodetector, Nano Lett. **12**, 2773 (2012).
[49] M. Bruna and S. Borini, Optical constants of graphene layers in the visible range, Appl. Phys. Lett. **94**, 031901 (2009).
[50] A. Yariv, P. Yeh, eds., *Optical Waves in Crystals: Propagation and Control of Laser Radiation* (Wiley-Interscience, New York, 1983).
[51] A. Ferreira, N. M. R. Peres, R. M. Ribeiro, and T. Stauber, Graphene-based photodetector with two cavities, Phys. Rev. B **85**, 115438 (2012).
[52] J.-T. Liu, H. Tong, Z.-H. Wu, J.-B. Huang, and Y.-S. Zhou, Greatly enhanced light emission of MoS_2 using photonic crystal heterojunction, Sci. Rep. **7**, 16391 (2017).
[53] J.-T. Liu, N.-H. Liu, L. Wang, X.-H. Deng, and F.-H. Su, Gate-tunable nearly total absorption in graphene with resonant metal back reflector, EPL (Europhys. Lett.) **104**, 57002 (2013).
[54] M. Qin, S. Xiao, W. Liu, M. Ouyang, T. Yu, T. Wang, and Q. Liao, Strong coupling between excitons and magnetic dipole quasi-bound states in the continuum in WS_2-TiO_2 hybrid metasurfaces, Opt. Express **29**, 18026 (2021).
[55] M. A. Vincenti, D. de Ceglia, M. Grande, A. D'Orazio, and M. Scalora, Nonlinear control of absorption in one-dimensional photonic crystal with graphene-based defect, Opt. Lett. **38**, 3550 (2013).
[56] A. Nematpour, N. Lisi, L. Lancellotti, R. Chierchia, and M. L. Grilli, Experimental mid-infrared absorption (84%) of single-layer graphene in a reflective asymmetric Fabry–Perot filter: Implications for photodetectors, ACS Appl. Nano Mater. **4**, 1495 (2021).
[57] J. Liu, M. Fan, K. Luo, Q. Yang, J. Li, and Z. Wu, Two-Dimensional Heterojunction Photovoltaic Cells with Low Spontaneous-Radiation Loss and High Efficiency Limit, Phys. Rev. Appl. **12**, 034023 (2019).
[58] H. Liu, S. Zhang, H. Ding, W. Sun, and L. Sun, Investigation on the optical dual-band absorption enhancement for graphene photodetector, Results Phys. **29**, 104747 (2021).
[59] H. Liu, W. Dong, H. Wang, L. Lu, Q. Ruan, Y. S. Tan, R. E. Simpson, and J. K. Yang, Rewritable color nanoprints in antimony trisulfide films, Sci. Adv. **6**, eabb7171 (2020).

[60] Q. Meng, X. Chen, W. Xu, Z. Zhu, S. Qin, J. Zhang, and X. Yuan, High q resonant graphene absorber with lossless phase change material Sb_2S_3, Nanomaterials **11**, 2820 (2021).

[61] N. V. Voshchinnikov, G. Videen, and T. Henning, Effective medium theories for irregular fluffy structures: Aggregation of small particles, Appl. Opt. **46**, 4065 (2007).

[62] Y. Chen, T.-S. Kao, B. Ng, X. Li, X. Luo, B. Luk'Yanchuk, S. Maier, and M. Hong, Hybrid phase-change plasmonic crystals for active tuning of lattice resonances, Opt. Express **21**, 13691 (2013).

[63] W. Dong, H. Liu, J. K. Behera, L. Lu, R. J. Ng, K. V. Sreekanth, X. Zhou, J. K. Yang, and R. E. Simpson, Wide bandgap phase change material tuned visible photonics, Adv. Funct. Mater. **29**, 1806181 (2019).

[64] J. W. Lichtman and J.-A. Conchello, Fluorescence microscopy, Nat. Methods **2**, 910 (2005).

[65] C. H. Camp Jr and M. T. Cicerone, Chemically sensitive bioimaging with coherent Raman scattering, Nat. Photonics **9**, 295 (2015).

[66] M. Ferrari and V. Quaresima, A brief review on the history of human functional near-infrared spectroscopy (FNIRS) development and fields of application, Neuroimage **63**, 921 (2012).

[67] J. He and Q. Zhang, An exact calculation of the Voigt spectral line profile in spectroscopy, J. Opt. A: Pure Appl. Opt. **9**, 565 (2007).